

# A SURVEY OF HYPERSONIC AERODYNAMICS AND AEROTHERMODYNAMICS FOR PLANETARY REENTRY CAPSULES

Chester Ong<sup>(1)</sup>, R.D. Braun<sup>(2)</sup>, and S.M. Ruffin<sup>(3)</sup>

<sup>(1-3)</sup> Georgia Institute of Technology, 270 Ferst Drive, Atlanta, GA 30332,

<sup>(1)</sup> Undergraduate, [g177i@mail.gatech.edu](mailto:g177i@mail.gatech.edu); <sup>(2)</sup> Professor, [Robert.braun@ae.gatech.edu](mailto:Robert.braun@ae.gatech.edu);

<sup>(3)</sup> Professor, [Stephen.ruffin@ae.gatech.edu](mailto:Stephen.ruffin@ae.gatech.edu);

## ABSTRACT

The purpose of this paper is to examine methods that analyze the hypersonic aerodynamics and aerothermodynamics for capsule reentry vehicles. The aerodynamic techniques covered are computational Newtonian, which include straight, modified, and Busemann-Newtonian. The aerothermodynamic approximations covered are the Sutton-Grave's and Chapman's Equations for stagnation point, convective heating rates; and the Lees-Dorodnitsyn's and Fay-Riddell's similarity transformations for convective heating along the body. Validation data includes three-dimensional and axisymmetric comparisons to Beagle-2, Mars Pathfinder, Stardust, and Apollo-4. The analysis hinges on the computations of GT-NASCART and CATIA. GT-NASCART is a CFD program for Windows or MAC developed at Georgia Tech. CATIA is a French-based CAD and mesher program. Additional topics covered – but in less, relative detail -- are planetary atmospheric conditions; post-shock calculations for equilibrium flow; viscous and boundary layer effects; trajectory effects; comparisons among half-angle cones and frontal radius; shape-change ablation; and hypersonic flow characteristics.

## 1. MOLECULAR INTERACTION OF AIR

The proceedings in this paper assume a continuum flow of local thermodynamic and chemical equilibrium. Continuum flow assumes that the mean molecular free path  $\lambda$  is small to the power of  $10^{-7}$  for altitudes below 92 km (earth) or when Knudsen Number  $Kn$  is less than a value of power  $10^{-4}$ . As altitude increases, density  $\rho$  decreases,  $\lambda$  increases to 0.3048 m at 100,000 m, and thus  $Kn$  increases. Between approximately 90 km and 150 km is the transitional regime, and above 150 km is the free-molecular flow regime. At  $100 > Kn > 1$ , the Euler and Navier-Stokes equations fail and “bridging” functions which account for the  $Kn$  are involved.

Equilibrium flow states that when density is sufficiently high and chemical reaction rates occur significantly faster than the “time scales of local fluid motion” [1] the infinite number of collisions among molecules produce a chemical equilibrium of reaction rates. Equilibrium flow is in contrast to frozen flow and non-equilibrium flow. Frozen flow assumes molecules cannot dissociate; that only one thermodynamic property is needed to uniquely define a state; and

generally acceptable up to low supersonic speeds. Nonequilibrium occur when molecules achieve insufficient collisions to produce equilibrium, i.e. during a strong shock wave (dissociation nonequilibrium) or rapid expansion (recombination nonequilibrium).

For earth conditions, air molecular weight is constant for altitudes below 100 km [1]. To determine freestream conditions based on geometric altitude, scale height, and atmospheric layers; the linear temperature and exponential density equations are utilized, with a less than 5% error *U.S. Standard Atmosphere 1976*

## 2. HYPERSONIC FLOW

Hypersonic flow occurs approximately after Mach 5. In this regime, the laws of supersonic aerodynamics change as significantly as subsonic to supersonic. A wedge at 15° degree angle of attack will produce an 18° shock wave [2]. Hypersonic flow possesses smaller  $\rho$ , thicker boundary layers, and a very thin shock layer that conducts a shock-viscous boundary layer interaction, where the viscosity significantly affects the pressures and heat rates, compared to supersonic flow.

### 2.1 Straight and Modified Newtonian Flow

After his postulate of  $F=ma$ , Newton egregiously theorized a stream of particles in rectilinear motion impacting a surface will lose all normal momentum but conserve all tangential momentum. While Newton's contemporary colleagues pigeonholed his fluid mechanics theory, Newton's later admirers noticed that his theory was well-suited for hypersonic flow – validating Newton's brilliant foresight -- where flow behaves ideally as a stream of particles.

In hypersonic aerodynamics, the pressure coefficient  $C_p$  is predicted only by local deflection angle  $\theta$  and only by surfaces directly in frontal flow contact: in Eq. 1,  $P$  is pressure;  $V$  is velocity; subscript 2 is post-shock conditions; and subscript  $\infty$  is freestream conditions.

$$C_p = \frac{P_2 - P_\infty}{\frac{1}{2} \rho_\infty V_\infty^2} = 2 \sin^2(\theta) \quad (1)$$

For blunted bodies, Lester Lees modified Eq.1 to Eq.2

$$C_{p,MOD} = C_{p,MAX} \sin^2(\theta) \quad (2)$$

where  $\gamma$  is effective ratio of specific heats,  $M$  is Mach, and  $C_{p,MAX}$  is given by Eq. 3. From  $C_p$  values, axial and

$$C_{p,MAX} = \frac{2}{\gamma M_\infty^2} \left\{ \left[ \frac{(\gamma+1)^2 M_\infty^2}{4\gamma M_\infty^2 - 2(\gamma-1)} \right]^{\gamma/(\gamma-1)} \left[ \frac{1-\gamma+2\gamma M_\infty^2}{\gamma+1} \right] - 1 \right\} \quad (3)$$

normal coefficients are calculated through integration. Eq. 2 will produce better results than Eq. 1 for blunted bodies. As Stardust and Apollo data will show, modified and straight Newtonian solutions produce values within 2% to 25% of each other. For high M and high geometric altitudes – earth case,  $M > 42$ , above 92km –  $\gamma$  approaches a value of one, equating the maximum  $C_p$  as value of two. For high M and high altitudes, Eq. 2 returns to its original form, that is Eq. 1.

### 2.1.2 Calculation of Post-shock $\gamma$

Eq. 1 only requires angle of attack  $\alpha$  and  $\theta$ . Eq. 2 additionally requires post-shock  $\gamma$  and freestream M. In hypersonics, isentropic functions are meaningless. Even with a “z” correction factor, Eq. 4 is useless, since the speed of sound equation is derived from temperature and pressure isentropic relations. The “z” correction factor accounts for molecular dissociation in hypersonic temperatures. In Eq. 4, variables are “a” speed of sound; P pressure; T temperature; and R Universal Gas Constant, 8314 (J/kg-mol·K). Instead,  $\gamma$  is computed

$$\gamma = \frac{\rho^* z^* a^2}{P} = \frac{z a^2}{RT} \quad (4)$$

by Eq. 5. Density ratio is calculated using an iterative solution of the continuity, momentum and energy conservation equations through enthalpy, pressure, and temperature tables from [3] and [4] for earth values.

$$\gamma = \frac{\eta + 1}{\eta - 1} - \frac{2\eta}{(\eta - 1)M_\infty^2}, \eta = \frac{\rho_2}{\rho_1} \quad (5)$$

### 2.2 Newtonian-Busemann Method

Eq. 1 and 2 are evaluated for a flat plate at an angle of inclination; through double or triple integration, Eq. 1 and 2 can evaluate curved surfaces. When the geometry is curved, however, a centrifugal force will act on the Newtonian fluid elements decreasing Newtonian pressure and introducing a centrifugal force term. Eq. 6 is a three-dimensional Newtonian centrifugal-force correction or Newtonian-Busemann.

$$C_p = 2 \sin^2 \theta_i + 2 \left( \frac{d\theta}{dy} \right)_i \frac{\sin \theta_i}{y_i} \int_0^{y_i} y \cos \theta dy \quad (6)$$

When Eq. 6 is plotted against straight Newtonian and numerical data over a circular cylinder flowing at hypersonic speeds with  $\gamma$  as 1.4, Fig. 1 displays straight Newtonian as more accurate to the numerical data from [1] than the Busemann method. The reason that Figure 7 displays a better reading for straight Newtonian and not centrifugal-corrected is not that Newtonian-hypersonic theory is faulty but rather that Newtonian-hypersonic theory operates best at infinite Mach numbers and a gamma equal to unity [2].

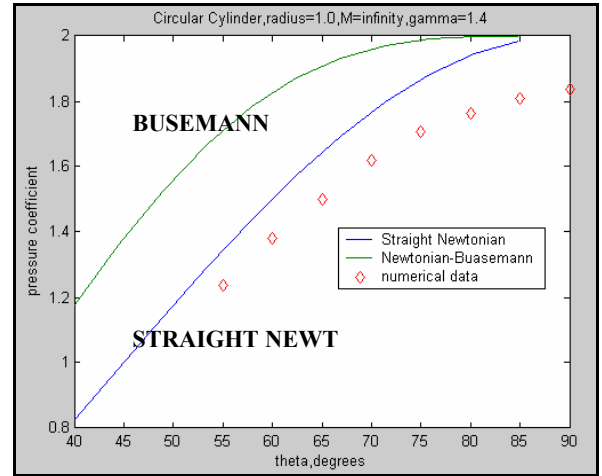


Fig. 1. Busemann method vs. Straight Newtonian

### 2.3 Tangent-Wedge, Cone Methods

The tangent-wedge and tangent-cone methods are methods (no general equations) that allow the prediction of surface pressure based on the assumption that local surface pressure is dependent on local surface inclination (similar to straight Newtonian flow) except with the inclusion of the hypersonic similarity parameter. The wedge method is valid only for 2-d shapes with constant slope, and the cone method is valid for slender axisymmetric shapes. The definition of “slender shapes” is an engineering “hand-wave.” While the –wedge and –cone methods are more accurate (to 4% in some cases), straight or modified Newtonian is very sufficient as a first degree approximation.

### 2.4 CATIA and GT-NASCART

GT-NASCART (CFD) provides a graphical and tabulated aerodynamic output for two-dimensional or three-dimensional, non-axisymmetric or axisymmetric, geometries for inviscid, Euler, Navier-Stokes, and straight or modified Newtonian solutions. CATIA provides the mesh points. The CPU time (for Dell9200) for GT-NASCART is 45 min. for linear, frontal triangle mesh (~3000 nodes, ~6000 elements); 15 min. for linear, frontal quadrilateral mesh (~3000 nodes, ~3000 elements); and the percent error between them is less than 0.4%. Using a parabolic mesh in CATIA produces incorrect results (reason unknown) in GT-NASCART.

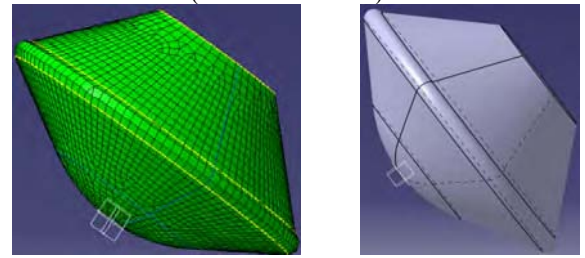


Fig 2. CATIA Beagle-2 Mesh (left) and Un-meshed (right)

### 3. AEROTHERMODYNAMICS

In hypersonic flow, vehicle heating becomes a primary concern. Temperatures behind the shock may reach 6000 K (ICBM) to 11,000 K (lunar return). Gas molecules dissociate from the extreme temperatures. At large entry velocities, such as 11 km/s, radiative heating becomes an important consideration: in the Apollo missions, the ratio between radiative heating to convective heating reached approximately 0.3 [2], requiring additional thermal protection systems (TPS).

Equ. 7 with constants C, M, and N accurately describe (to a first degree approximation) the heating rates along a body; the convective heating stagnation points; or the radiative heating points. C, N, and M are separate constants different for each application; and M in Eq. 7 is not for Mach number, as mentioned in Eq. 3.

$$|\dot{q}_w| = C\rho^N V^M \quad (7)$$

While molecular dissociation absorbs much of the energy and heat from the shock, the molecules may also re-associate post-shock, possibly at the vehicle outer geometry, releasing large amounts of heat. A non-catalytic surface prevents re-association of dissociated gas molecules at the body's outer geometry. The prevention of re-association precludes the release of energy and heat. However, a non-catalytic surface is useless if the molecules have re-associated before impacting the surface. A fully non-catalytic wall has a thermal conductivity (k) of zero; and a fully catalytic wall has k of near-infinity. When graphed against heat rate, a catalytic wall at equilibrium can experience a 70% greater convective heat rate than a non-catalytic wall. Direction Simulation Monte Carlo (DSMC) is required to create a bridging relation between non-catalytic and fully-catalytic against heat rate convection, although the pattern appears similar to the bridging functions of Knudsen numbers.

Viscous effects will affect the heat transfer to the vehicle. Transition from laminar to turbulent boundary layers will significantly increase the heat transfer, depending on the thickness of the boundary layer with respect to the body and the strength of the shock or shock-shock interaction wave. The effect of boundary layers at hypersonic speeds will also depend on the geometry configuration, angle of attack, and freestream conditions. A higher angle of attack will reduce the boundary layer, but increase the chance for shock detachment.

#### 3.1 Similarity Transformations

During his Ph.D. dissertation in 1908 to Dr. Prandtl, Dr. H. Blasius derived his famous "Blasius equation."

$$2f''' + ff'' = 0 \quad (8)$$

With f representing a function and tick marks representing derivatives, Eq. 8 allows partial differential equations to transform into ordinary differential equations. A similarity variable exists between any two properties if the properties subscribe to Eq. 8, the Blasius Solution. Due to page limits, the full derivations of the Fay-Riddell and Lees-Dorodnitsyn are left to the reader as well as the transformation works of R. Probstein, L. Lees [5], and van Driest.

#### 3.1.1 Fay and Riddell Transformation

The Fay-Riddle transformation Eq. 9 relates properties at coordinates (x,y) to similarity coordinates (S,η) with constant k as 1 for axisymmetric; k as 0 for 2-d; subscript w wall and e freestream-boundary layer edge; u velocity; r radius; and μ viscosity. The stagnation

$$\eta(x_1, y_1) = \frac{\rho_w u_e r_o^k}{\sqrt{2S}} \int_0^{y_1} \frac{\rho}{\rho_w} dy \quad (9)$$

$$S(x_1) = \int_0^{x_1} \rho_w \mu_w u_e r_o^{2k} dx$$

heat transfer rate (q dot) for laminar flow is Eq. 10 with Pr as Prandtl's number; H total enthalpy; h enthalpy in boundary layer; Le Lewis' number; subscript t as stagnation point value; and du/dx velocity gradient

$$\dot{q}_{stag} = \frac{0.763}{(\text{Pr}_{w,t})^{0.6}} (\rho_{t,2} \mu_{t,2})^{0.4} (\rho_{w,t} \mu_{w,t})^{0.1} \quad (10)$$

$$\cdot (H_{t,2} - h_{w,t}) [1 + (Le^{0.52} - 1) \frac{h_d}{H_{t,2}}] \left[ \left( \frac{du_e}{dx} \right)_{t,2} \right]^{0.5}$$

defined in Eq. 11. In Eq. 11, q infinity is freestream dynamic pressure and Φ is θ's complement angle.

$$\frac{du_e}{dx} = \frac{4q_\infty}{\rho_e u_e} \cos \phi \sin \phi \frac{d\phi}{dx} \quad (11)$$

#### 3.1.2 Lees-Dorodnitsyn Transformation

Eq. 12, Lees-Dorodnitsyn, relates properties at coordinate (x,y) to similarity coordinates (S,η)

$$\eta = \frac{\rho_e u_e r^k}{\sqrt{2\xi}} \int \frac{\rho}{\rho_e} dy \quad (12)$$

$$\xi = \int \rho_e \mu_e u_e r^{2k} dx$$

Eq. 13 is the heat rate along a sphere of radius r along length x for thermal conductivity k.

$$\dot{q} = \frac{k_w H_e}{c p_w} \left( \frac{u_e r \rho}{\sqrt{2 \rho_e \mu_e u_e r^2 x}} \right) g'(0) \quad (13)$$

Eq. 14 represents the heat rate along a cone of radius  $r$ ; half-angle  $\theta$ ; total stagnation  $H$  at boundary layer edge  $e$ ; and specific heat  $cp$  at constant pressure.

$$r = x \sin \theta$$

$$\dot{q} = \frac{k_w H_e \rho}{cp_w} \left( \frac{3u_e r}{2\rho_e \mu_e x} \right)^{0.5} g'(0) \quad (14)$$

Eq. 15 represents the value of  $g'(0)$  as the derivative of the ratio of total enthalpy to boundary layer (e) edge enthalpy. An integral solution to  $g'(0)$  is given in [5].

$$gw = g = \frac{H}{H_e}, \quad \frac{\partial g}{\partial \eta} = g'(0) \quad (15)$$

#### 4. MARS PATHFINDER & BEAGLE-2

In Table 1, for an axisymmetric body at zero angle, a less than ~2% error occurred for modified and straight Newtonian over a Mach range of 12 to 22 [6]. For Mach above 16, straight Newtonian produced a 2% less error than modified Newtonian, but at Mach below 12, straight Newtonian produced a 4% more error than modified Newtonian. As mentioned in Section 2.2, straight Newt operates best at infinite Mach and  $\gamma$  unity.

In Table 2, for a non-axisymmetric body at angles zero to 11, straight Newtonian produced far worse percent errors than Table 1 predictions. However, a 20% error in axial coefficient compared to [7] data is adequate for a 15-minute CFD Newtonian solution. The 66% error in normal coefficient is traced to the decimal place value required for adequate solutions.

Table 1: Mars Pathfinder Axisymmetric Drag Coefficients

angle 0 deg	Perfect Gas	Mod Newt.	Error	Straight Newt.	Error	$\gamma$
Mach	Euler, Hallis, CD	CD	%	CD	%	gamma
22.3	1.72	1.68	-2.21%	1.72	0.10%	1.0938
18.3	1.72	1.67	-2.36%	1.72	0.16%	1.101
16.0	1.71	1.67	-2.45%	1.72	0.32%	1.1105
12.2	1.68	1.66	-1.39%	1.72	2.23%	1.1405
9.4	1.64	1.64	0.23%	1.72	5.01%	1.18

Table 2: Beagle-2 Axial and Normal Coefficients, Mach 28

Beagle 2		CFD	straight		CFD	straight	
Minf	alpha	C <sub>A</sub>	C <sub>A</sub>	%	C <sub>N</sub>	C <sub>N</sub>	%
28	11	1.423	1.094	23.12%	0.095	0.1583	-66.63%
28	8	1.458	1.1058	24.16%	0.07	0.1165	-66.43%
28	5	1.475	1.114	24.47%	0.04	0.0734	-83.57%
28	2	1.484	1.1184	24.64%	0.019	0.0295	-55.26%
28	0	1.480	1.1193	24.37%	0.000	0	-

#### 5. APOLLO-4

Fig. 3-6 displays Apollo 4 aerodynamic coefficients comparisons among flight data and straight Newtonian. The flight data Mach number ranges from Mach 6 to 10, but little variation of aerodynamic coefficients against Mach number occurred after Mach 6 [8]. For Lift-to-Drag comparisons Fig 3, Newtonian theory agrees quite well with flight data, less than 10% error. In Fig 4, normal coefficients show a decreasing percent error as Apollo 4 capsule increases from 130 to 180 degrees – 31% to 24% error. In Fig. 5, the axial coefficient shows an increasing percent error as angle of attack increases – 9% to 22% error. In Fig 6, the moment coefficient shows a very poor correlation between flight data and numerical data, except for angles 170 and 180 degrees [9]. The reason for Figure 4 and 5 percent error is that as angle of attack increases, less total capsule area is covered by hypersonic Newtonian flow, and thus overestimation of aerodynamic data. The reason for Fig. 6 large percent error is that the moment center must be exact to obtain any reasonable moment coefficient percent error (less than 20%). The moment coefficient values dealt with are on the two to three decimal scale, and the CATIA model is a perfect geometry compared to the protrusions of Apollo-4. The smallest deviation of geometry could cause a significant percent error.

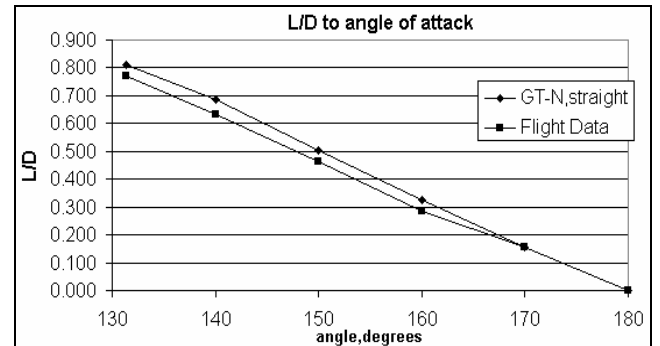


Fig 3. L/D vs. Angle of Attack

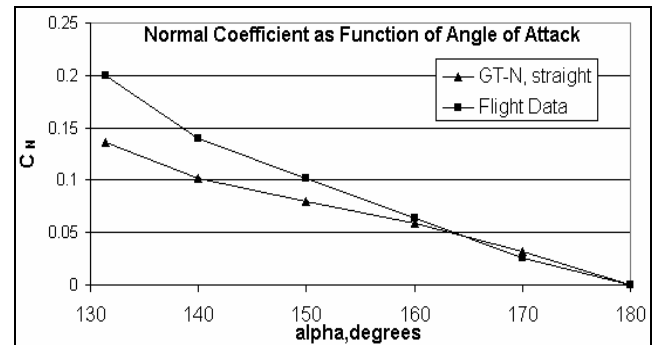


Fig 4. Normal Coefficient vs. Angle of Attack

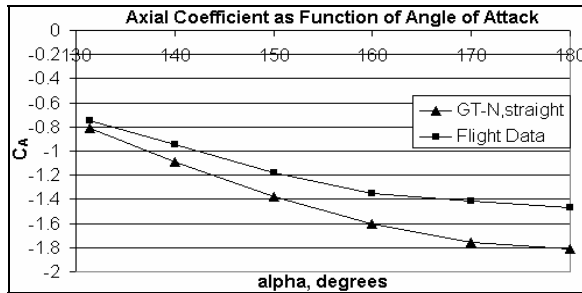


Fig 5. Axial Coefficient vs. Angle of Attack

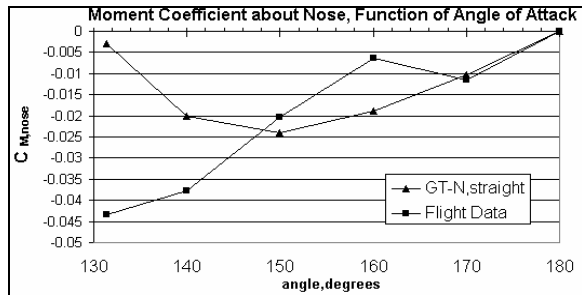


Fig 6. Moment Coefficient vs. Angle of Attack

## 6. STARDUST

### 6.1 Aerodynamic Data

For Fig. 7-10 graphs, Stardust aerodynamic coefficients are compared using NASA LAURA, straight Newtonian, and modified Newtonian solutions [10]. The percent error between straight to modified Newtonian aerodynamic coefficients is 5% average. The average percent error between modified Newtonian and NASA LAURA data is 4.17% for axial coefficients, 12.21% for normal coefficients, and 44.79% for moment coefficients. In Fig. 7, LAURA displays very little axial coefficient deviation between itself at Mach 35 and Mach 12. In Fig. 8, axial coefficients solutions vary greatly at low but not high Mach numbers. In Fig. 9, normal coefficients among straight Newtonian, modified Newtonian, and LAURA show good agreement with each other at 5 and 10 degrees angle, except at Mach 10. Fig. 10 moment coefficients represent the same large errors as in Fig. 6.

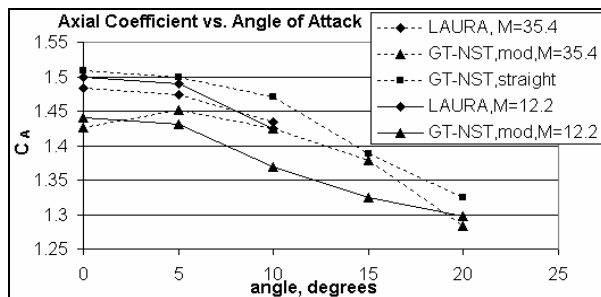


Fig 7. Axial Coefficient vs. Angle of Attack

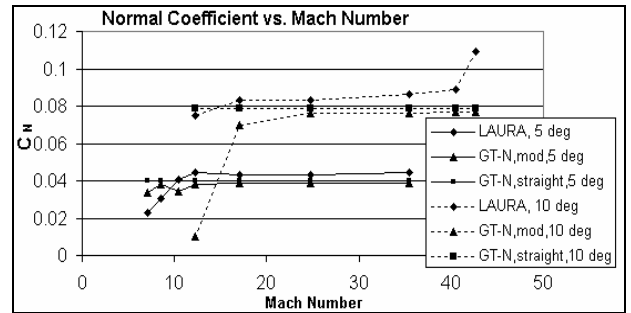


Fig 8. Axial Coefficient vs. Mach Number

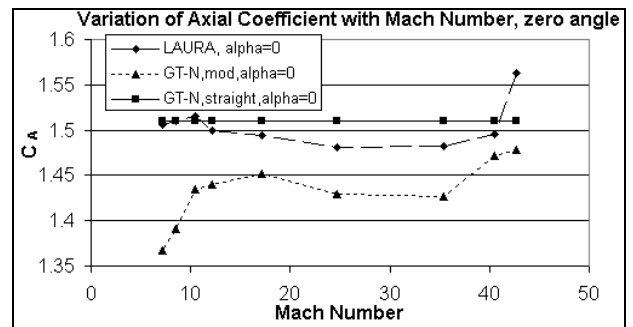


Fig 9. Normal Coefficient vs. Mach Number

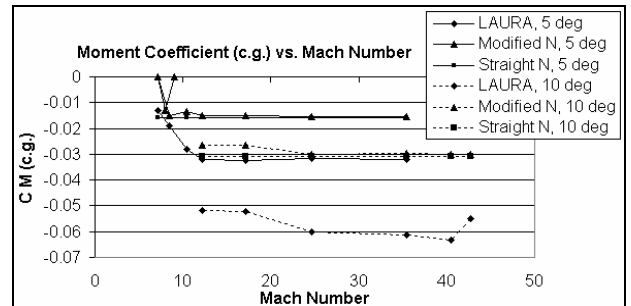


Fig 10. Moment Coefficient vs. Mach Number

### 6.2 Shape Change-Ablation

Under a maximum heat rate of 1200 W/cm<sup>2</sup>, the Stardust Capsule will recess its frontal area (diameter) and increase its nose radius due to TPS ablation at approximately Mach 40.5 at 70 km altitude and below [11]. Fig. 11 displays the change in pressure coefficients from the non-ablative Stardust to the ablative Stardust using a straight Newtonian solution. Fig. 11 is a graph of  $C_p$  versus Y-axes body location (not in cardinal order). The ablative Stardust  $C_p$  fall very closely with the non-ablative Stardust up to a Y value of 0.12 m, then begin to deviate across the frontal ~60 degree half-angle slope. The difference in  $C_A$  values between ablative and non-ablative capsules is 14%. Based on [11], the percent error in  $C_A$  values at zero angle of attack between ablative and non-ablative capsules is 1%. The GT-NASCART Stardust nose-section ablation change agrees with LAURA: 1%



change in aerodynamic coefficients. The frontal half-angle is the problem, which is after Y-position 0.10 on Figure 14. This 13% discrepancy between GT-NASCART and LAURA leads to the conclusion that (most likely) a user-input error for frontal half-angle occurred in CATIA, since the larger discrepancies begin after the nose radius. However, the percent error is approximately small so the cause may also stem from plain Newtonian-LAURA discrepancy.

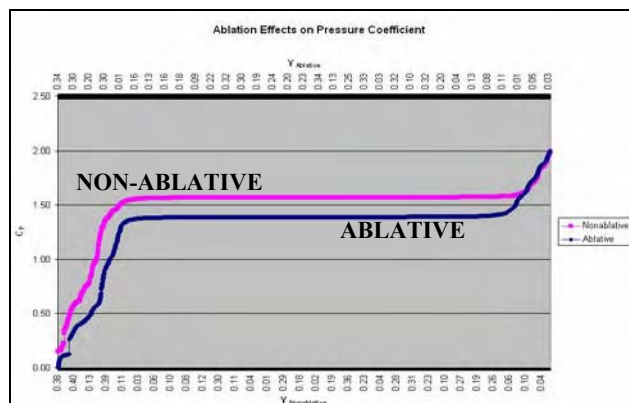


Fig 11. Ablation Effects:  $C_p$  versus Y-axes body location

## 7. CONCLUSION AND ACKNOWLEDGEMENTS

The importance of this paper is to review methods of analyzing hypersonic aerodynamics and aerothermodynamics. The methods of calculating aerodynamics involved straight Newtonian flow, modified Newtonian flow, Busemann-Newtonian flow, and tangent-wedge/cone methods. Based on validations to Stardust, Apollo-4, Beagle-2, and Mars Pathfinder data, the verdict for Newtonian measurement is that straight Newtonian is the best degree of approximation for hypersonics. The percent error between straight and modified Newtonian is within 5%, but the time to calculate post-gamma shock is inefficient. On average, Newtonian methods work best for high Mach, unity gamma, axial coefficients, and sometimes normal coefficients (15% error). Due to precise moment centers, Newtonian methods are not well-suited for moment coefficient calculations.

The methods for calculating heat rate involve the Sutton-Grave's, Chapman's Equation, Fay-Riddle Transformation, and Lees-Dorodnitsyn Transformation. The Sutton-Grave's and Chapman's Equations easily calculate the stagnation point, convective heat rate, given three constants, density, and velocity. For convective heat rate along a body, the Fay-Riddle Transformation calculates the stagnation point, convective heat rate based on air flow constants, boundary layer edge properties, and a velocity gradient that may relate to Newtonian flow. The Lees-

Dorodnitsyn Transformation calculates the convective heat rate along a sphere or cone. Validation of the F-R and L-D Transformations and the percent errors to flight data remains for future work.

I wish to thank my advisors at Georgia Tech, Professor Robert D. Braun and Professor Stephen M. Ruffin, for giving me this opportunity, and the graduate students at Georgia Tech's Space System Design Lab, for answering an undergraduate's plethora of questions.

## 8. REFERENCES

1. Bertin, John. *Hypersonic Aerothermodynamics*. AIAA Education Series 1994.
2. Anderson, John. *Hypersonic and High Temperature Gas Dynamics*. AIAA Series 2000.
3. Hansen, C.F. Approximations for the Thermodynamic and Transport Properties of High-Temperature Air, *NASA/NACA TR R-50*. Nov. 1957.
4. Moeckel, W.E. and Weston, K.C. Composition and Thermodynamic Properties of Air in Chemical Equilibrium, *NACA TN-4265*. April 1958.
5. Lees, Lester. Laminar Heat Transfer Over Blunt-Nosed Bodies at Hypersonic Flight Speeds. *Jet Propulsion*. April 1956. pp.259-269.
6. Gnoffo, P.A., et al. Effects of Sonic Line Transition on Aerothermodynamics of the Mars Pathfinder Probe. *AIAA 1998-2445*
7. Liever, P.A., et al. Computational Fluid Dynamics Prediction of the Beagle 2 Aerodynamic Database, *Journal of Spacecraft and Rockets*, Vol.40, No.5, September-October 2003.
8. Crowder, R.S., and Moote, J.D. Apollo Entry Aerodynamics, *Journal of Spacecraft and Rockets*, Vol. 6, No.3, March 1969 p.302-307.
9. Hillje, Ernest J. Entry Aerodynamics at Lunar Return Conditions Obtained from the Flight of Apollo 4 (AS-501), *NASA TN D-5399* October 1969.
10. Mitcheltree, R.A., Wilmoth, R.G., and Cheatwood, F.M. Aerodynamics of Stardust Sample Return Capsule. *AIAA 15<sup>th</sup> Applied Aerodynamics Conf.*, June 1997. p 697-707.
11. Wilmoth, R.G., Mitcheltree, R.A., Moss, J.N. Low-Density Aerodynamics of the Stardust Sample Return Capsule. *AIAA Paper 97-2510*
12. DeJarnette, F.R. and Hamilton, H.H. "A Review of Some Approximate Methods Used in Aerodynamic Heating Analyses." *Journal of Thermophysics*. Vol.1, No.1 Jan. 1987. p5-12.
13. van Driest, E.R. "The Problem of Aerodynamic Heating." *Aeronautical Engineering Review*. Oct. 1956. p.26-41.